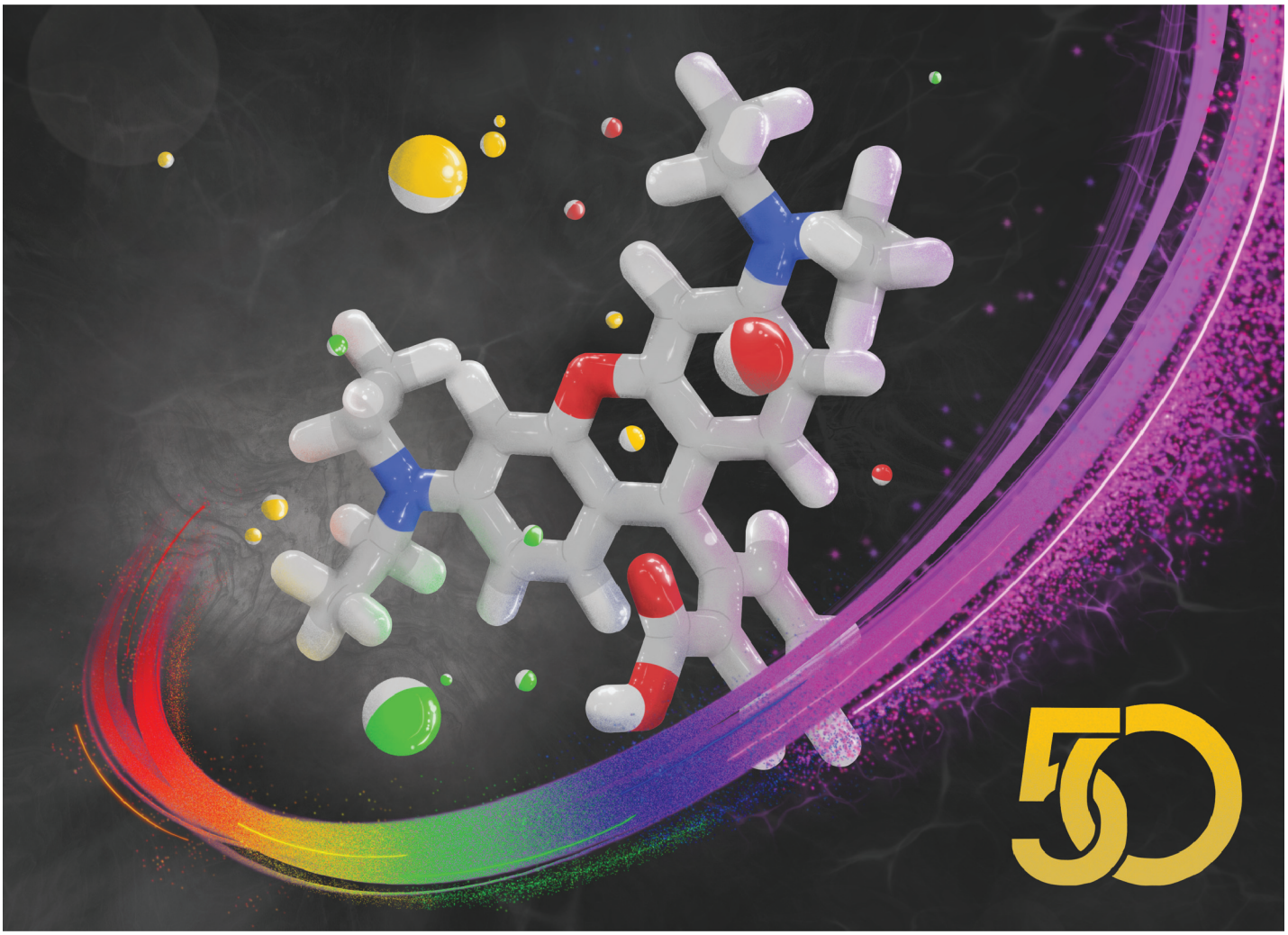

Showcasing research from the Colloidal Materials lab at the Institute of Materials Science of Seville (CSIC), Spain.

$NaY(MoO_4)_2$-based nanoparticles: synthesis, luminescence and photocatalytic properties

Undoped and lanthanide (Eu^{3+}, Tb^{3+} and Dy^{3+})-doped $NaY(MoO_4)_2$ nanoparticles with spherical shape have been synthesized, which show photocatalytic activity for dyes decomposition under visible light illumination. Moreover, under UV illumination, the doped systems, exhibit intense luminescence whose color is determined by the doping cation (red for Eu^{3+}, green for Tb^{3+} and yellow for Dy^{3+}).

As featured in:

See Manuel Ocaña *et al.*, *Dalton Trans.*, 2021, **50**, 16539.

ROYAL SOCIETY OF CHEMISTRY

rsc.li/dalton

Registered charity number: 207890

Dalton Transactions

ROYAL SOCIETY OF CHEMISTRY

PAPER

View Article Online
View Journal | View Issue

Cite this: *Dalton Trans.*, 2021, **50**, 16539

$NaY(MoO_4)_2$-based nanoparticles: synthesis, luminescence and photocatalytic properties†

Nuria O. Núñez, Elisabet Gómez-González, Roxana M. Calderón-Olvera, Ana I. Becerro, Gerardo Colón and Manuel Ocaña *

Received 16th July 2021,
Accepted 1st November 2021

DOI: 10.1039/d1dt02365a

rsc.li/dalton

We report on a novel synthesis method, which produces $NaY(MoO_4)_2$ nanoparticles having an almost spherical shape and hydrophilic character. The procedure is also suitable for the preparation of NaY $(MoO_4)_2$-based nanophosphors by doping this host with lanthanide cations (Eu^{3+}, Tb^{3+} and Dy^{3+}), which, under UV illumination, exhibit intense luminescence whose color is determined by the selected doping cation (red for Eu^{3+}, green for Tb^{3+} and yellow for Dy^{3+}). The effects of the cations doping level on the luminescent properties are analyzed in terms of emission intensities and luminescent lifetime, to find the optimum phosphors. Finally, the performance of these nanophosphors and that of the undoped system for the photocatalytic degradation of rhodamine B, used as a model compound, is also analyzed.

Introduction

Double rare earth (RE) based molybdates with the general formula $NaRE(MoO_4)_2$ and scheelite structure have found in the last years several interesting applications in different fields such as photocatalysis,[1] optoelectronics,[2,3] temperature sensing[4] and bioimaging.[5,6] In particular, uniform NaY $(MoO_4)_2$ micrometer sized particles have been shown to be a capable photocatalyst for organics degradation.[1] When doped with lanthanide cations (Ln^{3+}), $NaY(MoO_4)_2$ results in an efficient luminescent material with potential applications as lasers,[7] temperature sensors[8] and for anticounterfeiting technologies.[9] The main advantages of the $NaY(MoO_4)_2$ matrix over other matrices in Ln^{3+}-based phosphors are its high chemical and thermal stability as well as the high absorption coefficient of the $(MoO_4)^{2-}$ group, which has the ability to efficiently transfer the absorbed energy to the doping Ln^{3+} ions, resulting in an important improvement of their luminescence.[5,6]

For most of the above-mentioned applications, uniform particles in the nanometer size range are needed. For example, bioprobes for *in vivo* applications must be composed of uniform nanoparticles with a size <100 nm to avoid embolism and ensure sufficient circulation time.[10] In the photocatalysis field, it is expected that the increase of surface area associated with the particle size decrease might be beneficial for the catalytic performance.[11]

Ln-Doped $NaY(MoO_4)_2$ phosphors have been synthesized by a variety of procedures including hydrothermal/solvothermal procedures,[1,8,9,12–18] molten salts methods[19,20] and the conventional solid state reaction.[21] Most of the reported methods yielded particles with heterogeneous size and shape[11,12,17–20] or with uniform shape but in the micron size range.[1,13–16] Only Ding *et al.* have obtained uniform nanoparticles by a solvothermal procedure in the presence of oleic acid and oleylamine as capping agents.[22] However, such nanoparticles were hydrophobic as a consequence of the adsorption of such organic molecules on their surface, which precludes their use in some applications, unless they are rendered hydrophilic through post-synthesis ligand exchange strategies,[23,24] which in some cases affect the size, shape and composition of the particles.[23] Therefore, it remains as challenge to develop novel procedures for the synthesis of uniform Ln-doped $NaY(MoO_4)_2$ nanoparticles. Among different alternatives, the use of polyols as solvents in wet-chemical precipitation methods seems to be attractive, as polyols are known both to limit particle growth and to confer hydrophilic character to the precipitated particles.[5,6]

In this work, we report a method for the synthesis of uniform $NaY(MoO_4)_2$ nanoparticles with almost spherical shape and hydrophilic character by homogeneous precipitation from solutions of proper precursors in ethylene glycol/water mixtures. This procedure is shown to be also useful for the preparation of nanophosphors with tunable color by doping the molybdate matrix with Eu^{3+} (red), Tb^{3+} (green) or Dy^{3+} (yellow) cations, whose luminescent properties are studied in detail. Finally, the performance of these materials for the photocatalytic degradation of rhodamine B, used as a model compound, is also analyzed.

Instituto de Ciencia de Materiales de Sevilla (CSIC-US), c/Américo Vespucio, 49, 41092 Seville, Spain. E-mail: mjurado@icmse.csic

†Electronic supplementary information (ESI) available. See DOI: 10.1039/d1dt02365a

Experimental

Chemicals

Yttrium(III) nitrate hexahydrate ($Y(NO_3)_3{\cdot}6H_2O$, Sigma Aldrich 99.8%), europium(III) nitrate pentahydrate ($Eu(NO_3)_3{\cdot}5H_2O$, Sigma Aldrich 99.9%), dysprosium(III) nitrate hydrate ($Dy(NO_3)_3{\cdot}xH_2O$, Sigma Aldrich 99.9%) and terbium(III) nitrate hydrate ($Tb(NO_3)_3{\cdot}xH_2O$, Sigma Aldrich 99.9%) were use as rare earth precursors. Sodium molybdate (Na_2MoO_4, ≥98%, Sigma Aldrich) was used as molybdate source whereas ethylene glycol (EG, Sigma Aldrich, ≥99.5%) and Milli-Q water were used as solvent. Rhodamine B (Sigma Aldrich, <95%) was used for photocatalytic experiments.

Sample preparation

First, a weighted amount of $Y(NO_3)_3$ was dissolved in EG (2.5 mL) under magnetic stirring, heating the vial to temperatures close to 80 °C to facilitate the dissolution process. In a separate vial, Na_2MoO_4 was dissolved in a certain volume of water and EG was added to complete 2.5 mL of mixture. The latter solution was added to that containing the Y precursor, under magnetic stirring, and the mixture (total volume = 5 mL) was quickly introduced into a tightly closed test tube and heated in an oven preheated at 120 °C for 20 hours. The resulting dispersion was left to cool to room temperature, centrifuged to remove the supernatant, and the precipitate was washed twice with ethanol and once with distilled water. Finally, the obtained product was dispersed in Milli-Q water or, for some analyses, it was dried at room temperature.

For the synthesis of the Ln doped nanoparticles, the same procedure was used but adding the desired amount of the corresponding Ln nitrates to the $Y(NO_3)_3$ solution in EG, keeping the rare earth nitrate concentration in all final solutions at 0.02 mol L^{-1}. The Ln^{3+} content was varied between 2.5 and 25 mol% to investigate the effect of this magnitude on the luminescent properties and optimize the performance of the prepared nanophosphors.

Characterization

Transmission electron (TEM) and scanning electron (SEM) microscopy analyses were performed in a JEOL 2100Plus microscope and a Hitachi S4800 microscope, respectively. Energy-dispersive X-ray spectroscopy (EDS) analyses were carried out in a FEI Talos high-resolution transmission electron microscope.

Particle size distributions were estimated by counting several hundred particles from the TEM micrographs using free software ImageJ.

X-ray diffraction (XRD) patterns were obtained using a Panalytical X'Pert Pro diffractometer equipped with an X-Celerator detector. The determination of unit cell parameters from the XRD data (collected at intervals of 0.02° 2θ with an accumulation time of 1000 s) was carried out by Rietveld refinement using the X'Pert High Score Plus software. The starting parameters were taken from Stedman *et al.*[25] The crystallite size was estimated from the (2 0 4) reflection (2θ = 47.4°) using the Scherrer formula.

The infrared spectra (FTIR) of the powdered samples diluted in KBr pellets were recorded in a JASCO FT/IR-6200 Fourier Transform spectrometer.

BET surface area and porosity measurements were carried out by N_2 adsorption at −196 °C using a Micromeritics TristarII instrument.

Luminescent measurements (excitation and emission spectra and decay curves) were conducted in a Horiba Jobin Yvon spectrofluorometer (Fluorolog3) equipped with a Xenon lamp. For measuring the excitation and emission spectra, all samples were dispersed in water at the same concentration (0.5 mg mL^{-1}). The decay curves were recorded on powdered samples. Photographs of the samples deposited on Millipore filters were taken under daylight and UV (λ = 254 nm) illumination. The CIE chromaticity coordinates of the emitted light were calculated from the emission spectra using a 2° observer.

The photocatalytic activity was tested for rhodamine B (RhB) degradation using samples previously calcined at 400 °C for 1 h. RhB oxidation reactions were performed using a Pyrex immersion well reactor using a 200 W Xe lamp with a 420 nm cuttoff filter. Before each experiment, the catalysts (1 g L^{-1}) were settled in a suspension with the reagent mixture for 30 min in the dark. In the oxidation tests, an oxygen flow (15 mL min^{-1}) was used to produce a homogenous suspension of the catalyst in the solution. Before each photo-experiment, the catalysts were settled in suspension with the reagent mixture for 30 min in the dark. The evolution of the initial RhB concentration (5 ppm in water) was followed by UV-vis spectrometry through the evolution of its characteristic 553 nm band, using aliquots *ca.* 2 mL of the suspension previously centrifuged. The degradation rates were calculated from the slopes of the conversion plots at the first 60 min of reaction, and assuming a zero-order kinetics at this stage of the reaction. In all cases, RhB discoloration proceeds by chromophore cleavage because no significant shift was observed in their characteristic UV-vis bands followed by the photoactivity studies.

Results and discussion

Synthesis and characterization

The synthesis of undoped $NaY(MoO_4)_2$ nanoparticles was first addressed for simplicity. Initially, the $Y(NO_3)_3$ and Na_2MoO_4 concentrations in the final solutions were kept at 0.02 mol L^{-1} and 0.2 mol L^{-1}, respectively, whereas the reaction temperature and aging time were fixed at 120 °C and 20 h. As solvent, we used pure EG in a first attempt finding that the precipitate consisted of irregular, strongly aggregated particles (Fig. S1†). However, the addition of water to the EG solution (EG/H_2O volume ratio = 4/1) resulted in the precipitation of dispersed nanoparticles with a nearly spherical shape (Fig. 1, top) and a mean diameter of 51 nm (standard deviation, σ = 10) (Fig. 1, bottom).

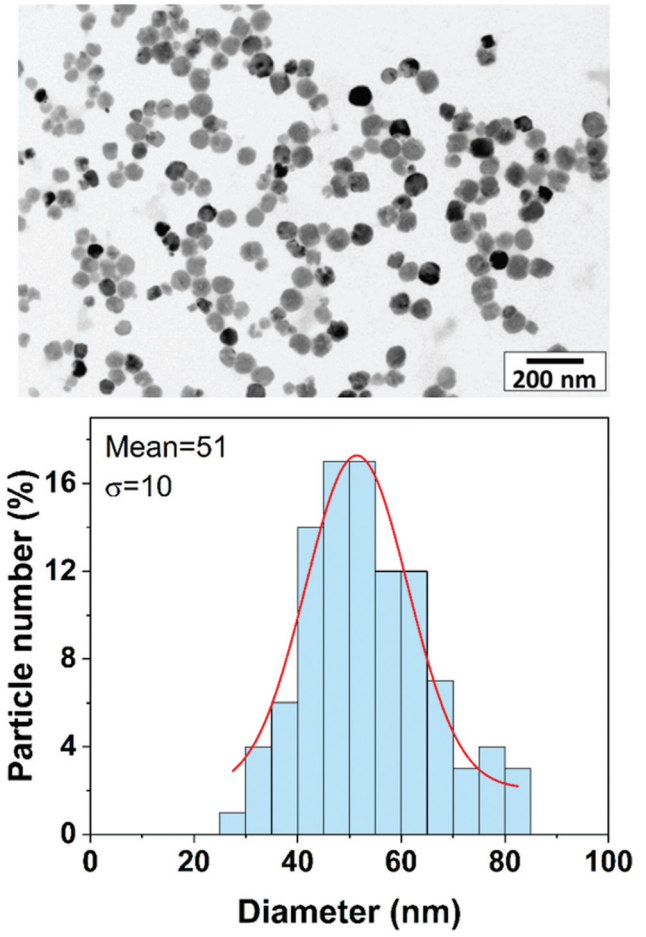

Fig. 1 TEM micrograph (top) and corresponding size histogram (bottom) of the particles obtained by aging at 120 °C for 20 h a solution in EG/H_2O (4/1 by vol) solvent containing 0.02 mol L^{-1} $Y(NO_3)_3$ and 0.2 mol L^{-1} Na_2MoO_4.

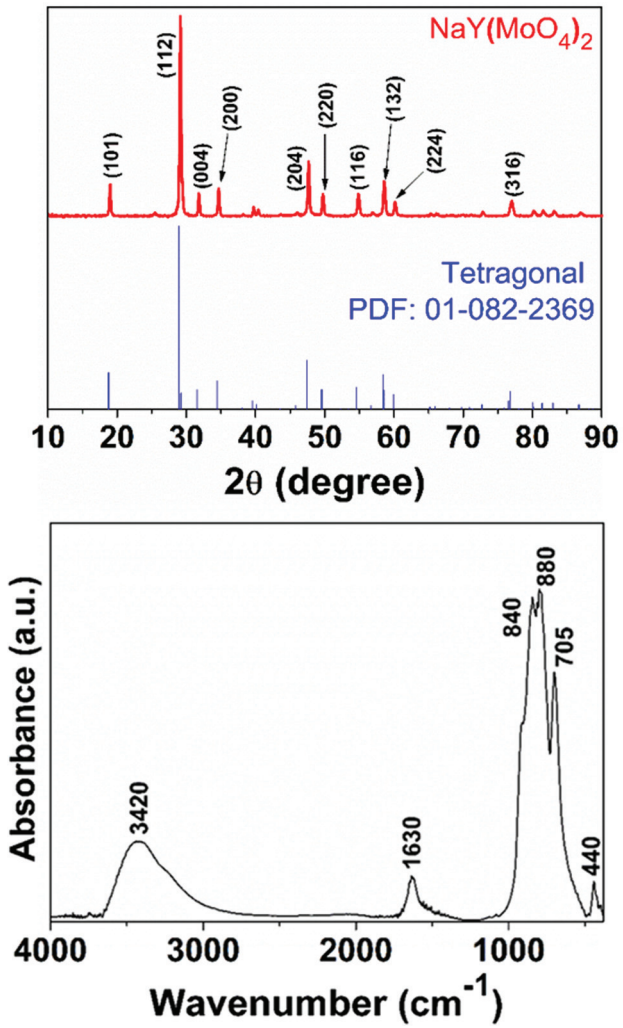

Fig. 2 XRD pattern (top) and FTIR spectrum (bottom) of the sample shown in Fig. 1.

It is important to note that the EG/H_2O volume ratio is an essential factor determining the uniformity of the precipitated particles since EG/H_2O ratios <4/1 as well as pure water rendered irregular particles (Fig. S1†). Likewise, the value of the MoO_4^{2-}/Y^{3+} molar ratio in the starting solutions was also critical since ill-defined precipitates were also obtained when reducing the molybdate anions concentration (Fig. S2†). Such morphological differences may be attributed to changes in the kinetics of nucleation and particle growth induced by different viscosity and dielectric constant of the reaction media according to the classical LaMer and Dinegar model.[26]

X-ray diffraction indicated that the nanospheres were crystalline with tetragonal $NaY(MoO_4)_2$ structure (Fig. 2, top). The crystallite size obtained using the Scherrer formula was very similar (47 nm) to the particle size estimated from the TEM micrographs, suggesting that the nanospheres presented a monocrystalline character. Finally, FTIR spectroscopy revealed a high purity for this sample since only bands at about 3420 and 1630 cm^{-1}, due to adsorbed water could be detected in the spectrum (Fig. 2, bottom) in addition to the lattice vibrations modes (bands at <1000 cm^{-1}) corresponding to $NaY(MoO_4)_2$.[27]

Ln-Doped (Ln = Eu, Tb or Dy) $NaY(MoO_4)_2$ nanoparticles (Ln:$NaY(MoO_4)_2$) were synthesised using the same protocol as that succeeded for the synthesis of the undoped system, which was only modified by introducing the desired amounts of Ln precursors into the starting solutions. It was found that the morphology of the particles was not affected by the doping procedure, irrespective of the selected Ln^{3+} cation (Eu^{3+}, Tb^{3+} or Dy^{3+}) (Fig. S3, S4 and S5†). However, a decrease of mean particle diameter (in most cases ≤40 nm) was detected for all systems when compared with the undoped sample (51 nm), which was more marked for the Eu doped samples (Table 1). This behaviour has been previously observed for other Ln-doped systems synthesised by wet chemical methods and it has been tentatively justified based on the effects of Ln^{3+} cations on the energetic barriers involved in the precipitation event.[6]

Table 1 Mean diameter (nm) and standard deviation (in parenthesis) of the $NaY(MoO_4)_2$ nanoparticles doped with different amounts of Ln^{3+} cations

Doping cation	Eu^{3+}	Tb^{3+}	Dy^{3+}
2%			40(7)
5%	42(9)	47(9)	42(8)
10%	26(6)	38(12)	42(7)
15%	25(5)	36(9)	41(11)
20%	26(6)	33(10)	
25%	24(11)	24(4)	

XRD patterns of all doped samples displayed exclusively the reflections corresponding to tetragonal $NaY(MoO_4)_2$ (Fig. S6†) indicating the purity of the samples. Elemental distribution maps obtained by EDS showed the homogeneous distribution of the Ln doping cations into the NPs (Fig. S7†). The incorporation of such cations into the $NaY(MoO_4)_2$ crystal structure forming a solid solution was confirmed by unit cell parameters measurements. Thus, a progressive increase of the unit cell volume with increasing Ln^{3+} doping level was observed for all three dopants (Fig. 3), which suggests the substitution of Ln^{3+} cations for Y^{3+} in agreement with the higher ionic radii of Eu^{3+} (1.066 Å), Tb^{3+} (1.040 Å) and Dy^{3+} (1.027 Å) when compared with Y^{3+} (1.019 Å). The differences in ionic radii also justify that the observed increase in cell parameters was higher for the Eu^{3+} system and almost negligible for the Dy^{3+} doped one.

Luminescent properties

The excitation spectra of all Eu^{3+} doped samples were similar to that shown in Fig. 4a, which corresponds to 5% Eu^{3+} content. In agreement with previous reports,[11] it consisted of several weak and narrow bands mainly in the 350–400 nm wavelength region, corresponding to the direct excitation of the Eu^{3+} cations from the ground state to the higher energy levels labelled in the figure, along with a much broader band centred at 285 nm, which evidences the presence of an energy transfer (ET) process from the molybdate anions to the Eu^{3+} cations.[11] The much higher intensity of this band when compared to those corresponding to the direct excitation indicated that the ET process is the most convenient excitation path for this system.

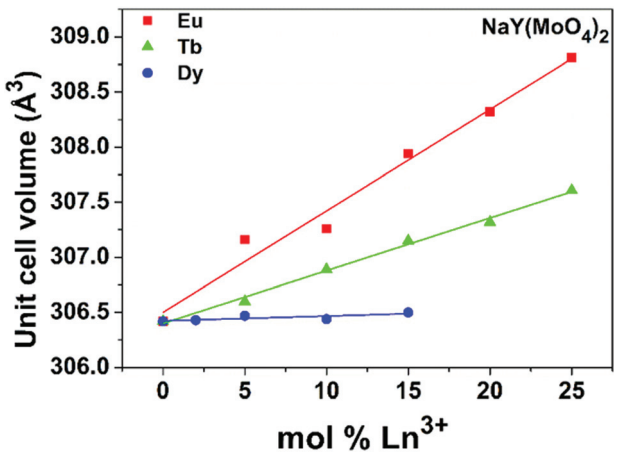

Fig. 3 Unit cell volume of the Ln-doped $NaY(MoO_4)_2$ samples as a function of the doping level.

The emission spectra of the Eu-doped samples were consequently recorded by excitation through the ET band (Fig. 4b). As expected, all spectra were similar to each other and displayed the bands corresponding to the characteristics $^5D_0$–^7F_j (j = 1, 2, 3, 4) transitions of the Eu^{3+} cations.[11] The highest emission intensity was detected at 616 nm. This band gave rise to the emission of intense red light (Fig. 5a), whose chromatic coordinates are shown in Fig. 5b. Such coordinates were the same for all essayed Eu^{3+} doping level.

Fig. 4c displays a plot of the integrated area of the emission spectra as a function of the Eu^{3+} content. The emission intensity increased with increasing Eu doping level from 5 to 20% as a consequence of the increase in the number of emitting centres. However, the emission intensity remained practically unaltered when the Eu content was raised to 25%. This observation suggests the presence of the well-known concentration quenching effect, produced by cross relaxation processes among emitting centers (Eu^{3+} ions in this case) which are located close to each other in the $NaY(MoO_4)_2$ crystal structure.[28] To shed more light on the presence of such a phenomenon, we analysed the dynamics of the luminescence by recording decay curves for all Eu-doped samples at the dominant emission wavelength of Eu^{3+} (616 nm, $^5D_0 \rightarrow {}^7F_2$ transition) (Fig. 4d). Although very similar to each other, a close observation of the curves allows observing that they became progressively shorter with increasing Eu content. To quantify the luminescence decays, the curves were fitted using a bi-exponential temporal dependence of the form:

$$I(t) = I_{01}\exp(-t/\tau_1) + I_{02}\exp(-t/\tau_2) \quad (1)$$

where $I(t)$ is the luminescence intensity, t is the time after excitation and τ_i (i = 1, 2) is the decay time of the i-component, with intensity I_{0i}. Bi-exponential decays are typical of lanthanide-doped nanoparticles. The long-lifetime component is generally assigned to the intrinsic decay time of emitting lanthanide centres in the interior of the nanoparticle while the short-lifetime component is related to the decay of lanthanides near the surface, which are influenced by quenchers such as surface defects, ligands or solvent molecules. The corresponding fitting parameters are summarized in Table 2 together with the average decay time, $\langle\tau\rangle$, calculated as:

$$\tau = \frac{\int_0^\infty tI(t)\mathrm{d}t}{\int_0^\infty I(t)\mathrm{d}t} = (\tau_1{}^2 I_{01} + \tau_2{}^2 I_{02})/(\tau_1 I_{01} + \tau_2 I_{02}) \quad (2)$$

The $\langle\tau\rangle$ values progressively decreased with increasing Eu^{3+} content (Table 1), which indicates that concentration quenching is taking place already at low Eu doping levels.

From these data it can be concluded that the 5% Eu-doped sample is the most efficient nanophosphor, as it shows the highest lifetime value. However, the sample doped with 20%

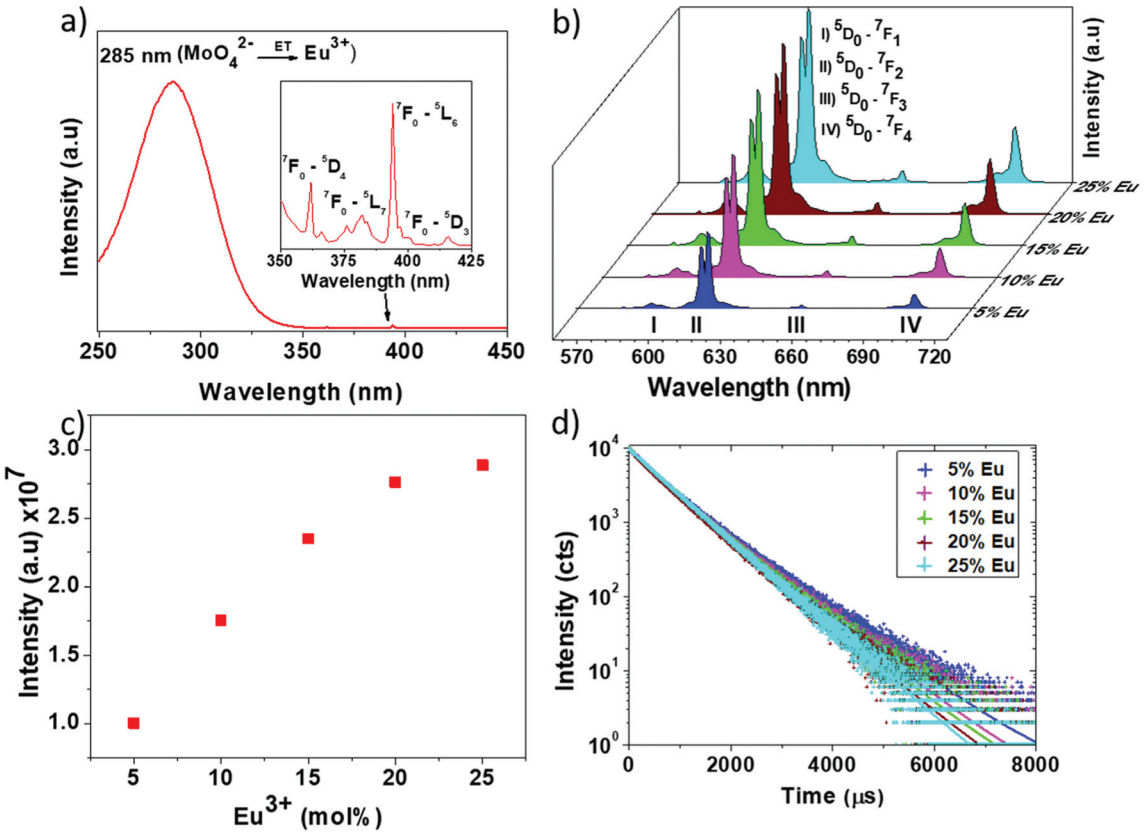

Fig. 4 (a) Excitation spectrum of the Eu(5%):$NaY(MO_4)_2$ nanophosphor monitored at 616 nm; (b) emission spectra obtained on excitation at 285 nm for the Eu:$NaY(MO_4)_2$ nanophosphors having different Eu content; (c) integrated intensity of the Eu^{3+} emissions plotted as a function of the Eu content; (d) decay curves for the $^5D_0 \rightarrow {}^7F_2$ transition of Eu^{3+} obtained for the samples having different Eu content.

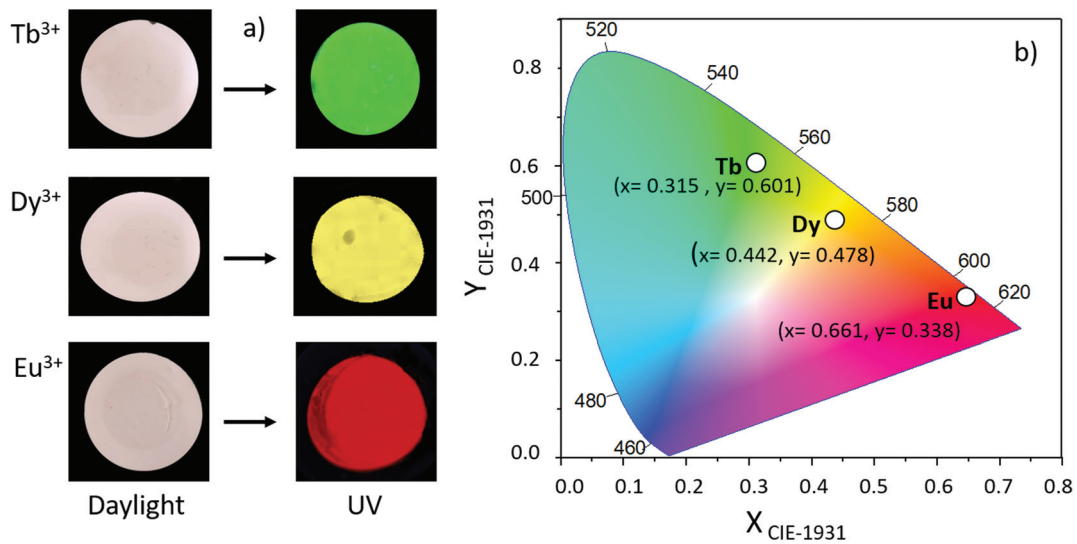

Fig. 5 (a) Photographs of the powdered Ln-doped $NaY(MoO_4)_2$ nanophosphors deposited on Millipore filters taken under daylight and UV (λ = 254 nm) illumination. (b) CIE-1931 *x*–*y* diagram showing the chromaticity coordinates of the luminescent light under UV excitation.

Eu^{3+} seems more appropriate for applications as it showed the highest emission intensity. This apparent discrepancy must be ascribed to a partial compensation of the emission intensity decrease due to the concentration quenching effect by the intensity increase expected from the increasing number of emitting centres.

Table 2 Lifetime values (τ_1 and τ_2) of the I_{01} and I_{02} components and average lifetimes values ($\langle\tau\rangle$) obtained for the Ln:NaY$(MoO_4)_2$ nanophosphors from the $^5D_0 \rightarrow {}^7F_2$ (Eu^{3+}), $^5D_4 \rightarrow {}^7F_5$ (Tb^{3+}) and $^4F_{9/2} \rightarrow {}^6H_{13/2}$ (Dy^{3+}) transitions, after pulsed excitation (λ_{ex} = 385 nm) as a function of the Ln content

% Ln	I_{01} (%)	τ_1 (μs)	I_{02} (%)	τ_2 (μs)	$\langle\tau\rangle$ (μs)
5% Eu	25	435	75	895	830
10% Eu	22	439	78	828	777
15% Eu	22	456	78	799	751
20% Eu	16	390	84	766	732
25% Eu	10	459	90	738	719
5% Tb	28	163	72	682	638
10% Tb	32	141	68	634	587
15% Tb	36	153	64	617	560
20% Tb	45	141	55	560	489
25% Tb	56	126	44	514	421
2% Dy	22	49	78	249	238
5% Dy	22	58	78	232	221
10% Dy	21	49.6	79	207	198
15% Dy	23	28	77	156	149

The excitation spectra of the Tb^{3+} doped samples (Fig. 6a) resembled that of the Eu^{3+} doped ones, showing several weak bands in the 350–400 nm region due to the f–f electronic transitions within the Tb^{3+} levels (labelled in the figure), along with a similar ET band at 285 nm, in agreement with previous reports.[11] When excited at the later wavelength, several bands in the green region characteristic of the $^5D_4$–^7F_j (j = 6, 5, 4, 3) Tb^{3+} transitions were detected (Fig. 6b), with the highest emission at 543 nm, responsible for the green colour of the emission (Fig. 5a), as observed in the chromaticity coordinates plot (Fig. 5b), which were invariant with the Tb content. The integrated intensity of the emission spectra became higher with increasing the Tb doping level from 5 to 15% and decreased for higher Tb contents (Fig. 6c). This behaviour clearly revealed the presence of concentration quenching, which is more pronounced than in the Eu-doped system, in agreement with previous reports.[27,29]

The luminescence decay curves recorded for the Tb^{3+}:NaY$(MoO_4)_2$ samples at the characteristic emission of Tb^{3+} (540 nm, $^5D_4 \rightarrow {}^7F_5$) showed shorter curves with increasing Tb content (Fig. 4d). Indeed, the average lifetime values obtained after fitting the curves to a bi-exponential function, as in the case of the Eu-system shown above, showed a progressive decrease with increasing Tb doping level (Table 1), which reveals the presence of concentration quenching at the studied Tb content range. In summary, also in this case, the lifetime values indicate that the most efficient nanophosphor is that doped with 5% Tb while the highest emission intensity was recorded for the sample doped with 15%, which is therefore the most adequate nanophosphor for applications.

Finally, the excitation spectra of the Dy-doped samples (Fig. 7a) displayed a set of narrow bands due to the f–f electronic transitions within the Dy^{3+} cations (from 330 to

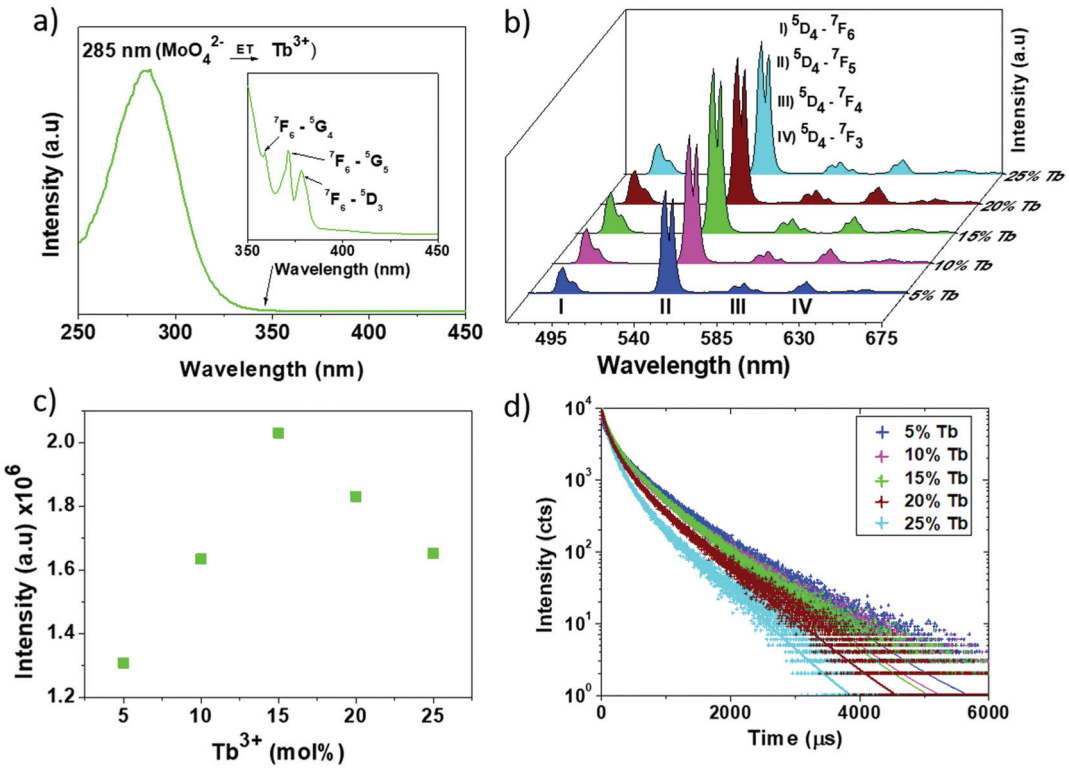

Fig. 6 (a) Excitation spectrum of the Tb(5%):NaY$(MO_4)_2$ nanophosphor monitored at 543 nm; (b) emission spectra obtained on excitation at 285 nm for the Tb:NaY$(MO_4)_2$ nanophosphor having different Tb content; (c) integrated intensity of the Tb^{3+} emissions plotted as a function of the Tb content; (d) decay curves for the 540 nm, $^5D_4 \rightarrow {}^7F_5$ transition of Tb^{3+}, obtained for the samples having different Tb content.

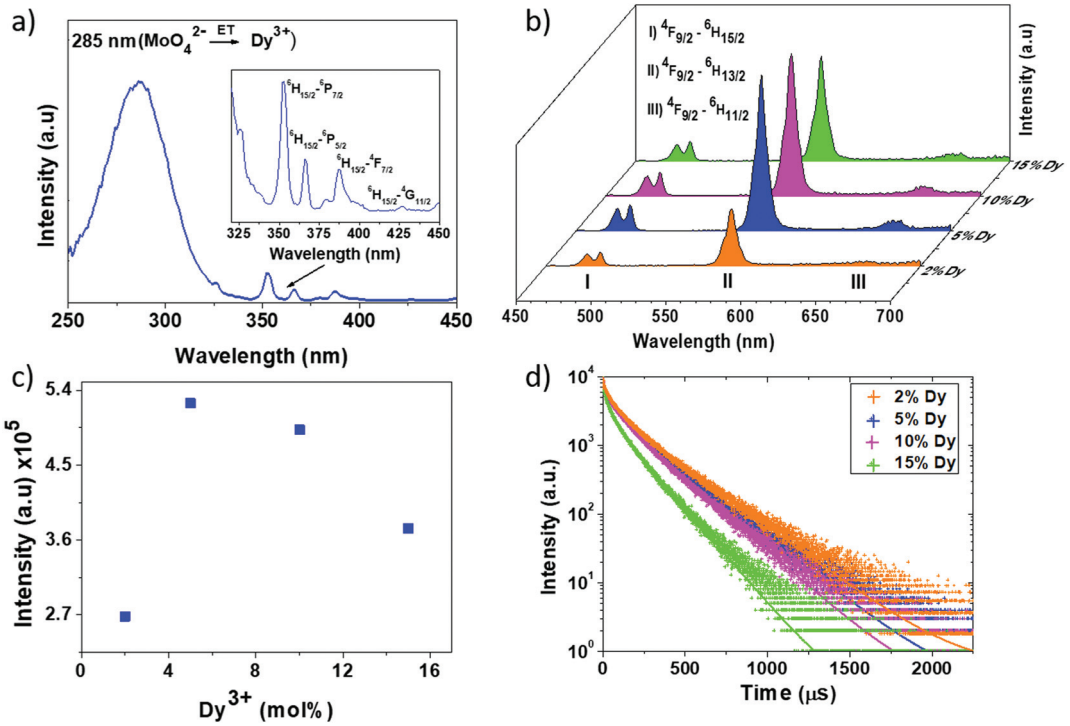

Fig. 7 (a) Excitation spectrum of the Dy(5%):NaY$(MO_4)_2$ nanophosphor monitored at 573 nm; (b) emission spectra obtained on excitation at 285 nm for the Dy:NaY$(MO_4)_2$ nanophosphors having different Dy content; (c) integrated intensity of the Dy^{3+} emissions plotted as a function of the Dy content; (d) decay curves for the 540 nm, $^4F_{9/2} \rightarrow {}^6H_{13/2}$ transition of Dy^{3+} obtained for the samples having different Dy content.

400 nm) and a broad ET band (285 nm)[12] similar to that observed for the Eu and Tb-doped systems here considered. Irrespective of the Dy^{3+} doping level, all spectra showed the bands corresponding the characteristics $^4F_{9/2}$–^6H_j (j = 15/2, 13/2, 11/2) transitions of the Dy^{3+} cations (Fig. 7b), the most intense one appearing at 573 nm, which resulted in a yellow luminescence (Fig. 5a) whose chromaticity coordinates are plotted in Fig. 5b.

The emission concentration quenching effect was also observed for these nanophosphors, the sample with the highest emission intensity being, in this case, the one doped with 5% Dy (Fig. 7c), which is a much lower value than that associated with the Eu and Tb-based systems. In agreement with this observation, the lifetime values of the Dy-doped samples, obtained from the bi-exponential fitting of their decay curves recorded for the $^4F_{9/2} \rightarrow {}^6H_{13/2}$ transition (Fig. 7d), decreased progressively with increasing Dy content (Table 1). This result reveals the presence of cross relaxation processes among Dy^{3+} ions which are close together in the NaY$(MoO_4)_2$ crystal structure, giving rise to the concentration quenching effect observed from the emission spectra. In this case, therefore, the most efficient nanophosphor is the 2% Dy-doped sample while the most appropriate for applications is that doped with 5% Dy, as it shows the highest emission intensity.

Photocatalytic properties

We have studied the photocatalytic performance of samples for RhB degradation under visible illumination, as in a previous report,[1] for comparison purposes. For this study, we have used both, undoped and Ln^{3+} (Ln = Eu, Tb or Dy)-doped $NaYMoO_4$ nanoparticles since the photocatalytic properties of previously reported molybdate-based materials has been found to be affected by Ln^{3+} doping cations.[30] As a case of study, we selected samples containing the same amount (5%) of doping cations.

Before performing the photocatalytic experiments, all samples were calcined at 400 °C for 1 h. After this treatment, no significant changes either in particle size and shape (Fig. S8†) or in crystalline structure (Fig. S9†) were detected. The BET analysis of the calcined series (Fig. S10†), revealed that lanthanide incorporation does not affect the isotherm shape. However, a certain effect on the BET surface area values can be highlighted. Thus, while undoped NaY$(MoO_4)_2$ showed a surface area of *ca.* 30 $m^2\ g^{-1}$, a slight increase of this magnitude was noticed for doped systems, the maximum increment being observed for the Eu-doped system (Fig. S8†). This effect would be in agreement with the smaller size of the doped nanoparticles when compared with the undoped ones.

The photocatalytic performance of the NaY$(MoO_4)_2$ samples for the photodegradation of RhB is shown in Fig. 8. From the evolution of the concentration with irradiation time (Fig. 8 top), it can be observed that all samples show certain photoactivity for dye degradation. This degradation process can be fitted to pseudo-first-order kinetics, and the values of the apparent first-order rate constants k_{app} are equal to the corresponding slope of the fitting line (Fig. 8 bottom). It was also

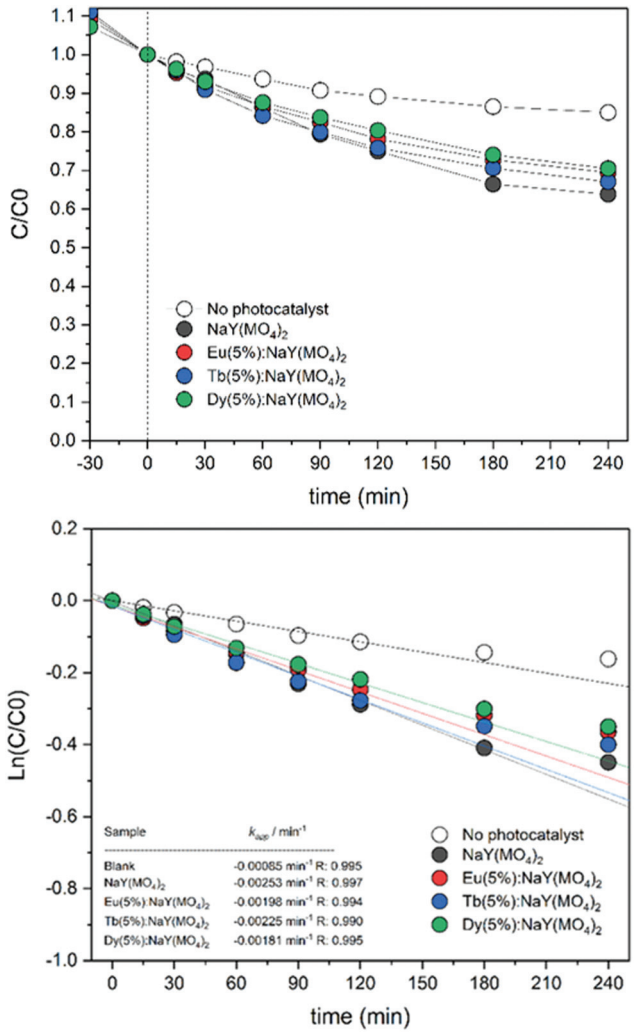

Fig. 8 Photocatalytic degradation of RhB over $NaY(MoO_4)_2$ systems: (top) degradation rate of RhB *versus* reaction time; (bottom) calculated k_{app} constants.

detected that a 40% degradation was achieved after 240 min in the case of undoped system, whereas the incorporation of lanthanide dopants leads to a slight decrease in the photoactivity, whose origin is unknown although it cannot be ascribed to NPs surface area variations since this magnitude was lower for the undoped sample. Nevertheless, it is important to mention that RhB degradation has been achieved in our case for particles with equiaxed morphology, which had no photocatalytic activity according to the previous report,[1] which might be related to the much higher surface area of our system. It must be mentioned that the photocatalytic activity of our NPs is lower than that previously reported for $NaY(MoO_4)_2$ micrometer sized particles with plate-like morphology (90%) although an exhaustive comparison of both data cannot be carried out since the operational conditions (especially that concerning the lamp power) differs substantially in both cases.[1] In summary, from these results, we could evidence that $NaY(MoO_4)_2$ nanoparticles here developed might be also interesting candidates for photocatalytic pollutant degradation.

Conclusions

Nearly spherical nanoparticles of a rather narrow size distribution consisting of tetragonal $NaY(MoO_4)_2$ have been obtained by low temperature (120 °C) homogeneous precipitation in an ethylene glycol/water mixture containing $Y(NO_3)_3$ and Na_2MoO_4. The solvent composition is a key factor to obtain uniform nanoparticles since by varying the ethylene glycol/water ratio, irregular and strongly aggregated particles were obtained. It is also shown that this procedure is suitable for the synthesis of lanthanide (Eu^{3+}, Tb^{3+} or Dy^{3+})-doped $NaY(MoO_4)_2$ nanoparticles with a shape similar to that of the undoped system and smaller size. Such doped systems exhibited strong luminescence under UV illumination, whose colour ranged from red (for Eu^{3+}) to green (for Tb^{3+}) and yellow (for Dy^{3+}). The most intense luminescence resulted for samples doped with 20% Eu, 15% Tb and 5% Dy, which can be considered as the optimum nanophosphors. It was also found that the undoped $NaY(MoO_4)_2$ nanoparticles show a significant capability for the photocatalytic degradation of rhodamine B under visible light, although a 5% lanthanide doping slightly decreased the photocatalytic activity.

In summary, because of the luminescence and photocatalytic properties of these $NaY(MoO_4)_2$-based nanoparticles, they might find interesting applications as nanophosphors for optical applications and as photocatalysts for the degradation of pollutants.

Conflicts of interest

There are no conflicts of interest to declare.

Acknowledgements

Funding from FEDER/Ministerio de Ciencia, Innovación y Universidades – Agencia Estatal de Investigación (grant RTI2018-094426–B-I00) and Junta de Andalucia (grant P20_00182) is acknowledged. R. M. Calderón-Olvera acknowledges financial support from the CONACYT-770734 postdoctoral grant. E. Gómez-González acknowledges the financial support from the FPI program (PRE2019-090170).

References

1 S. S. Liu, D. P. Yang, D. K. Ma, S. Wang, T. D. Tang and S. M. Huang, *Chem. Commun.*, 2011, **47**, 8013–8015.
2 S. B. Stevens, C. A. Morrison, T. H. Allik, A. L. Rheingold and B. S. Haggerty, *Phys. Rev. B: Condens. Matter Mater. Phys.*, 1991, **43**, 7386–7394.
3 T. Wang, S. Wang, H. Zhang, X. Zou and W. Hu, *Opt. Mater.*, 2020, **104**, 109851.

4 A. Li, D. Xu, H. Lin, S. Yang, Y. Shao and Y. Zhang, *Sci. Rep.*, 2016, **6**, 31366.
5 M. Laguna, N. O. Núñez, V. Rodríguez, E. Cantelar, G. Stepien, M. L. García, J. M. de la Fuente and M. Ocaña, *Dalton Trans.*, 2016, **45**, 16354–16365.
6 M. Laguna, N. O. Núñez, A. I. Becerro, G. Lozano, M. Moros, J. M. de la Fuente, A. Corral, M. Balcerzyk and M. Ocaña, *J. Colloid Interface Sci.*, 2019, **554**, 520–530.
7 A. Schmidt, S. Rivier, V. Petrov, U. Griebner, X. Han, J. M. Cano-Torres, A. García-Cortés, M. D. Serrano, C. Cascales and C. Zaldo, *J. Opt. Soc. Am. B*, 2008, **25**, 1341–1349.
8 L. Tang, Q. Meng, W. Sun and S. Lü, *J. Lumin.*, 2021, **230**, 117728.
9 X. Zhang, J. Wu, P. Wang, J. Gao, F. Gao and D. Gao, *Dalton Trans.*, 2021, **50**, 7826–7834.
10 X. Duan and Y. Li, *Small*, 2013, **9**, 1521–1532.
11 A. Kubacka, M. Fernández-García and G. Colón, *Chem. Rev.*, 2012, **112**, 1555–1614.
12 Z. Xu, C. Li, G. Li, R. Chai, C. Peng, D. Yang and J. Lin, *J. Phys. Chem. C*, 2010, **114**, 2573–2582.
13 Y. Huang, L. Q. Zhou, L. Yang and Z. W. Tang, *Opt. Mater.*, 2011, **33**, 777–782.
14 J. Liu, B. Xu, C. Song, H. Luo, X. Zou, L. Hana and X. Yu, *CrystEngComm*, 2012, **14**, 2936–2943.
15 Y. Li, G. Wang, K. Pan, W. Zhou, C. Wang, N. Fan, Y. Chen, Q. Feng and B. Zhao, *CrystEngComm*, 2012, **14**, 5015–5020.
16 L. Xu, X. Yang, H. Lu, C. Hu and W. Hou, *RSC Adv.*, 2014, **4**, 13502–13508.
17 Y. Li and X. Liu, *Mater. Sci. Eng., B*, 2014, **188**, 20–25.
18 H. Zheng, B. Chen, H. Yu, J. Sun, X. Li, J. Zhang, H. Zhong, Z. Wu and H. Xia, *RSC Adv.*, 2015, **5**, 56337–56347.
19 X. Zhang, Y. Liu, Y. Lu, B. Li, F. Song and F. Yang, *J. Mater. Sci.: Mater. Electron.*, 2015, **26**, 2987–2994.
20 L. Bai, Q. Meng, M. Huo and Y. Sui, *J. Rare Earths*, 2019, **37**, 1261–1268.
21 P. K. Tawalare, V. B. Bhatkar, R. A. Talewar, C. P. Joshi and S. V. Moharil, *J. Alloys Compd.*, 2018, **732**, 64–69.
22 Y. Ding, J. Liu, M. Zeng, X. Wang, J. Shi, W. Wang, Y. Miao and X. Yu, *Dalton Trans.*, 2018, **47**, 8697–8705.
23 A. Dong, X. Ye, J. Chen, Y. Kang, T. Gordon, J. M. Kikkawa and C. B. Murray, *J. Am. Chem. Soc.*, 2011, **133**, 998–1006.
24 N. Liu, N. Gobeil, P. Evers, I. Gessner, E. M. Rodrigues and E. Hemmer, *Dalton Trans.*, 2020, **49**, 16204–16216.
25 N. J. Stedman, A. K. Cheetham and P. D. Battle, *J. Mater. Chem.*, 1994, **4**, 707–711.
26 V. K. LaMer and R. H. Dinegar, *J. Am. Chem. Soc.*, 1950, **72**, 4847–4854.
27 Y. Wang, M. Song, L. Xiao and Q. Li, *J. Lumin.*, 2021, **238**, 118203.
28 X. Yang, Z. Fu, C. Zhang, Z. Wu and T. Sheng, *J. Mater. Sci.: Mater. Electron.*, 2015, **26**, 6659–6666.
29 Y. Tian, B. Chen, B. Tian, J. Sun, X. Li, J. Zhang, L. Cheng, H. Zhong, H. Zhong, Q. Meng and R. Hua, *Phys. B*, 2012, **407**, 2556–2559.
30 H. Li, W. Li, F. Wang, X. Liu and C. Ren, *Appl. Catal., B*, 2017, **217**, 378–387.